Electronic Modulation of Pd/C by Simultaneous Doping of Cu and Co Tendering a Highly Durable and Methanol-Tolerant Oxygen Reduction Electrocatalyst

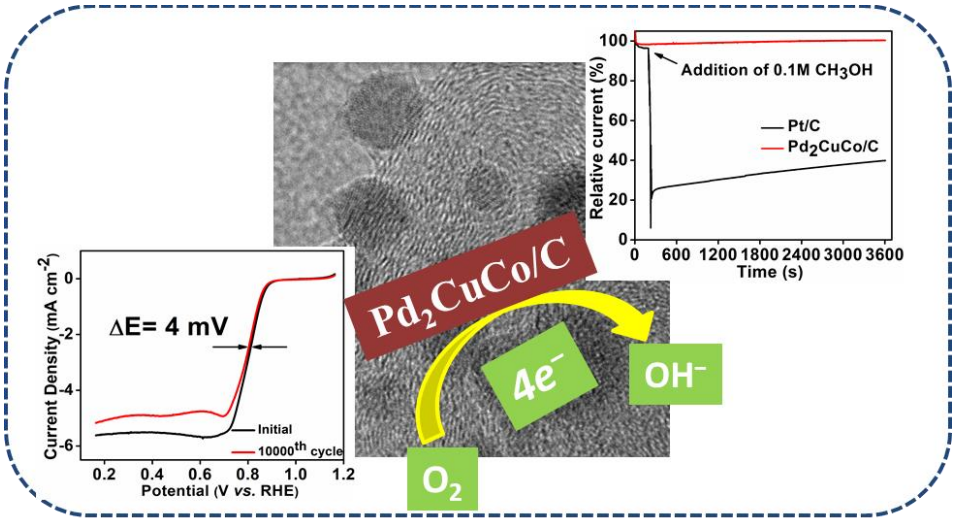

This chapter discusses a simple one-step solvothermal synthesis of a Pd_2CuCo/C for ORR electrocatalysis. The TEM data showed that Pd_2CuCo metallic counterparts is uniformly dispersed throughout the carbon support without aggregation, demonstrating the higher stability and less mass transfer resistance of the NPs. Homogeneous dispersion of metal NPs on carbon materials leads to higher active sites. A study combining several electrochemical studies shows that Pd_2CuCo/C acts as an efficient, long-lasting, and stable electrocatalyst towards ORR in an alkaline medium. The bimetallic electrocatalysts were also synthesized, and their ORR performances were examined to explore the synergistic and promotional impacts of Cu and Co on Pd. These results summarizes that the activity and utilization efficiency of Pd in electrochemical reactions can be increased by alloying with Cu and Co. The experimental procedures for the synthesis, characterization techniques, and electrocatalytic measurements were described in Chapter 2.

(*The content of this chapter has been published in "Energy & Fuels, 37(13): 9557–9567, 2023")

4.1. Introduction

Fuel cells (FCs) and metal-air batteries have been the subject of extensive research due to the growing desire for clean, efficient, environmentally friendly and sustainable energy conversion technologies [1-4]. Since the only byproducts released from FCs are heat and H_2O, Pt-based nanomaterials have been considered the ideal electrocatalysts for FCs, which would be the next generation of technology in the fields of transportation, stationary devices, and portable power production [1, 2, 3, 5-7]. However, Pt-based electrocatalysts' high cost, limited supply, short methanol endurance, and long-term instability limit their widespread application. Numerous investigations have been conducted to substitute less costly metals, including Pd, for Pt in FC applications [8–10]. Pd-based electrocatalysts are attractive alternatives for FC reactions owing to their higher natural abundance, identical lattice constant and comparable activity to Pt [11–14]. While Pd has emerged as a potential replacement for Pt in FC processes, developing monometallic Pd with good electrocatalytic performance towards ORR is challenging due to its electronic structure, which is not conducive enough to exhibit efficient transfer of electron during the ORR [15–17]. Many investigations have focused on improving its performance. One of the more successful approaches is to alloy Pd with other transition metals, such as Cu, Co, Fe, Ag, Ni, etc. [17-23]. According to the well-known "volcano plots," Cu and Co are located close to Pd, which supplies the right amount of binding energy to bond oxygen and good ORR performance. Moreover, compared to other metals in the "volcano plots," both are plentiful and economical. Therefore, research into Cu and Co-based catalysts are vital for ORR [18-20]. Alloying Pd with Cu and Co results in the strain effect and ligand effect. These two effects can modify the electronic structure of Pd, which ultimately accelerates ORR. Compressive strain in Pd may result from adding transition metals with smaller atomic sizes, such as Co and Cu. In addition to shortening the Pd-Pd bond length, the compressive strain also causes the center of the Pd-Pd band to move downward, optimizing O_2 adsorption and activation for increased ORR performance [18-24]. Furthermore, using conductive carbon materials like Vulcan carbon will boost its ORR activity by enabling metal NPs to be evenly distributed and stabilized. Consequently, it is anticipated that the Pd-based ternary alloy supported on conductive carbon will show more significant ORR catalytic activity and improved durability due to the interaction of the alloy effect and support effect [18-19]. Based on this understanding, recent research has been done to develop Pd-based alloy electrocatalysts with enhanced

catalytic performance [23-28]. For example, Wang *et al.* found that the nanothorn PdCuAu electrocatalysts exhibited improved catalytic activity, stability, and methanol tolerance for ORR [23]. In another study, nanoring-shaped PdPtCo electrocatalysts, synthesized through a template-directed method, showed significantly improved ORR activity due to their high edge-to-surface ratio and optimized composition [24]. In the same way, the trimetallic alloys, such as PdPtCu [25], PdPtFe [26], and PdPtNi [27] have shown remarkable electrocatalytic activity for ORR. Drawing inspiration from the above-mentioned research works, in this chapter we report a facile method to synthesize carbon-supported Cu and Co-doped Pd electrocatalysts with admirable ORR activity and long-term durability. The combination of appropriate Cu and Co with Pd metal engendered an effective compressive strain effect, and the support of Vulcan carbon increases the conductivity of the electrocatalysts.

4.2. Results and Discussion

4.2.1. Characterization of the Pd_2CuCo/C, PdCu/C and PdCo/C

The crystalline behavior and phase purity of the as-synthesized NPs were investigated by powder XRD analysis. Figure 4.1a represents the XRD patterns of the Pd_2CuCo/C and Pd/C NPs. From XRD, it is observed that the peaks located at 40°, 47°, and 68° correspond, respectively, to the (111), (200), and (220) crystallographic facets of Pd according to the JCPDS 89-4897. The diffraction patterns of Pd_2CuCo/C are shifted toward higher angles relative to the pure Pd/C, and the absence of XRD peaks corresponding to Co and Cu indicates the alloy formation caused by the introduction of smaller atomic radii of Co and Cu into the *fcc* lattice of Pd [29-32]. The additional diffraction peak present at 2θ of ~42° is attributed to the (002) plane of Cu_2O (JCPDS 65-3288). A broad diffraction peak located at ~25° ascribes to the (002) facet of Vulcan XC-72R (JCPDS 75-1621). From Bragg's law, the values of cell parameters (a) and d-spacing (d) were calculated based on the high intensity (111) peak of Pd. It is observed that the Pd_2CuCo/C exhibits comparatively smaller values of d (0.2230 nm) and a (0.3861nm) than Pd/C (d = 0.2254 nm and a = 0.3904 nm), indicating the lattice contraction of Pd owing to the Pd_2CuCo/C formation.

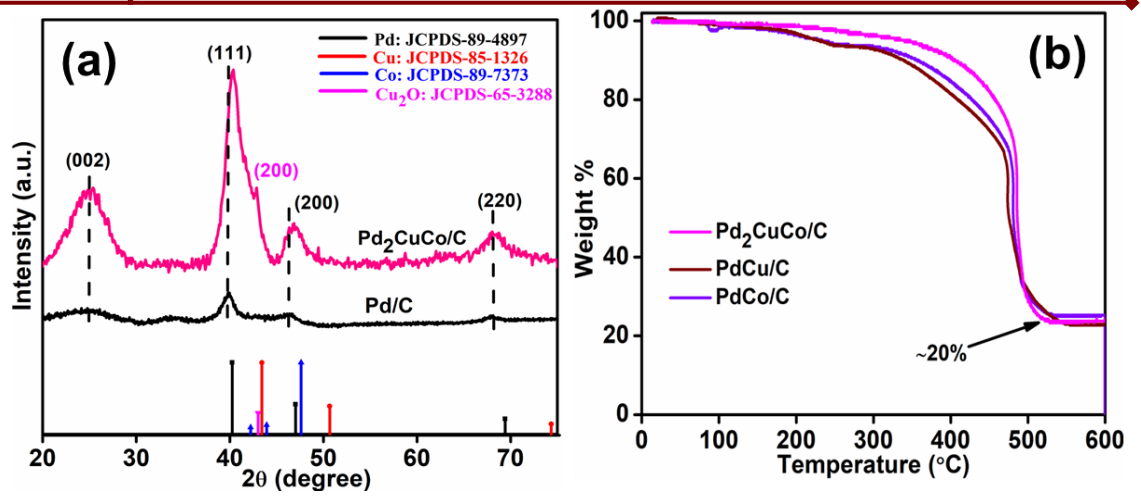

Figure 4.1: (a) X-ray diffraction patterns of Pd_2CuCo/C and Pd/C and (b) TGA profile of Pd_2CuCo/C, PdCu/C and PdCo/C.

TGA analysis in the air environment confirmed the metal loading over the carbon support (Figure 4.1b). The weight loss observed at about ~350°C due to transformation of carbon to CO_2 in the adequate air environment. The residue obtained after burning all the carbon compounds gives information about the total percentage of metal loading. The metal loading observed is ~20% in the Pd_2CuCo/C, PdCu/C and PdCo/C equivalent to the theoretically calculated total metal loading on the carbon support. EDX spectroscopy was used to evaluate the elemental composition in the synthesized electrocatalysts (Figure 4.2). The EDS elemental maps and the corresponding electron images show the distribution of metals over the carbon support. The estimated atomic percentages of Pd (2.46%), Co (1.05%), and Cu (1.74%) are in a 2:1:~1 ratio which corroborates well with the theoretically calculated value. Only the elements Pd, Co, Cu, and C are detectable in the synthesized electrocatalysts, indicating that the sample is highly pure. The weight percentages ratio of Pd_2CuCo over the carbon matrix resembles well with the TGA plot confirming the metal and support are in 20:80 ratio.

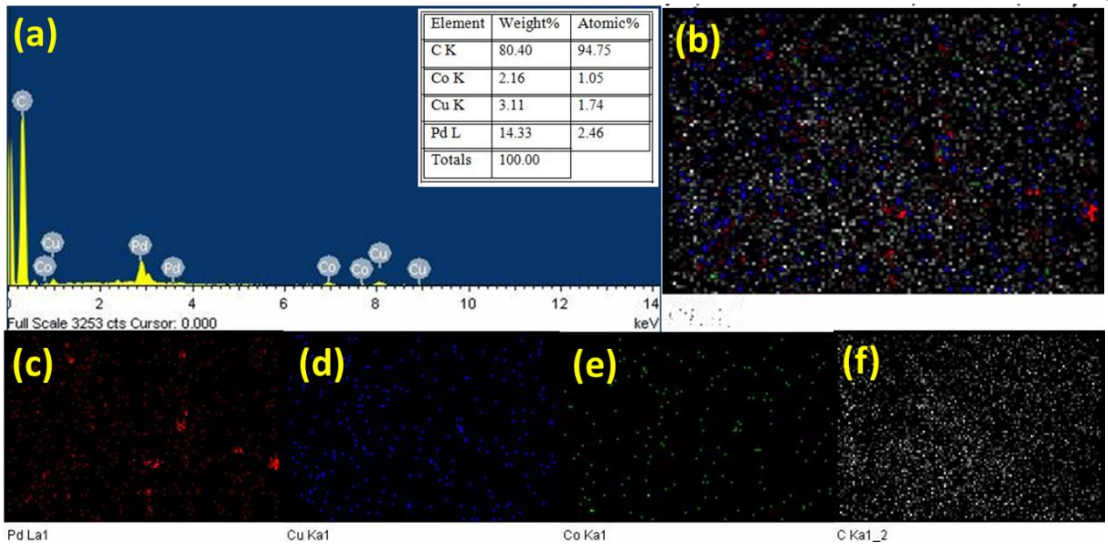

Figure 4.2: (a) EDX spectrum of Pd_2CuCo/C (inset: shows the table for elemental composition), (b) The overlayer image of C, Pd, Cu and Co, (c)-(f) elemental maps for individual Pd, Cu, Co, and C, respectively.

XPS analysis was carried out to investigate the chemical composition and oxidation state of elements present in Pd_2CuCo/C. Figure 4.3a presents the survey spectrum of the Pd_2CuCo/C and reveals the existence of Pd, Co, Cu, C, and O atoms. The Pd 3d spectrum could be fitted with four components, including two sets of strong and weak peaks (Figure 4.3b). The high-intensity peaks, emerging at binding energy (BE) of 335.3 and 341.2 eV were attributed to Pd(0) $3d_{5/2}$ and Pd(0) $3d_{3/2}$, respectively [32,33]. The other two weaker peaks that emerged at BE of 337.9 and 342.8 eV could be ascribed to the Pd(II) $3d_{5/2}$ and Pd(II) $3d_{3/2}$, respectively [34, 35]. It is expected that the occurrence of Pd(II) peak is due to the oxidation of Pd atoms on the surface of the NPs in ambient environments. The XPS pattern of Co 2p is shown in Figure 4.3c and the BE of the Co 2p peaks displayed a significant shift in comparison to the 778.3 and 793.2 eV of the typical metallic Co XPS peaks. The peaks observed at 785.3 and 802.8 eV are due to the oxidation of Co to CoO on the surface of the Pd_2CuCo/C NPs [35, 36]. The peaks of Cu are associated with Cu(0)/Cu(I) located at 932 and 951.9 eV, respectively, that correlate to Cu $2p_{3/2}$ and Cu $2p_{1/2}$ (Figure 4.3d). These peaks are slightly negatively shifted in contrast to the typical Cu 2p peaks (932.6 and 952.5 eV) indicating the coexistence of Cu(0)/Cu(I). Three very weak peaks were also observed at 933.7, 943.8 and 954.3 eV, indicating the presence of Cu(II) oxide which is due to the partial oxidation of the Pd_2CuCo/C surface exposed to the air atmosphere [28,35,37].

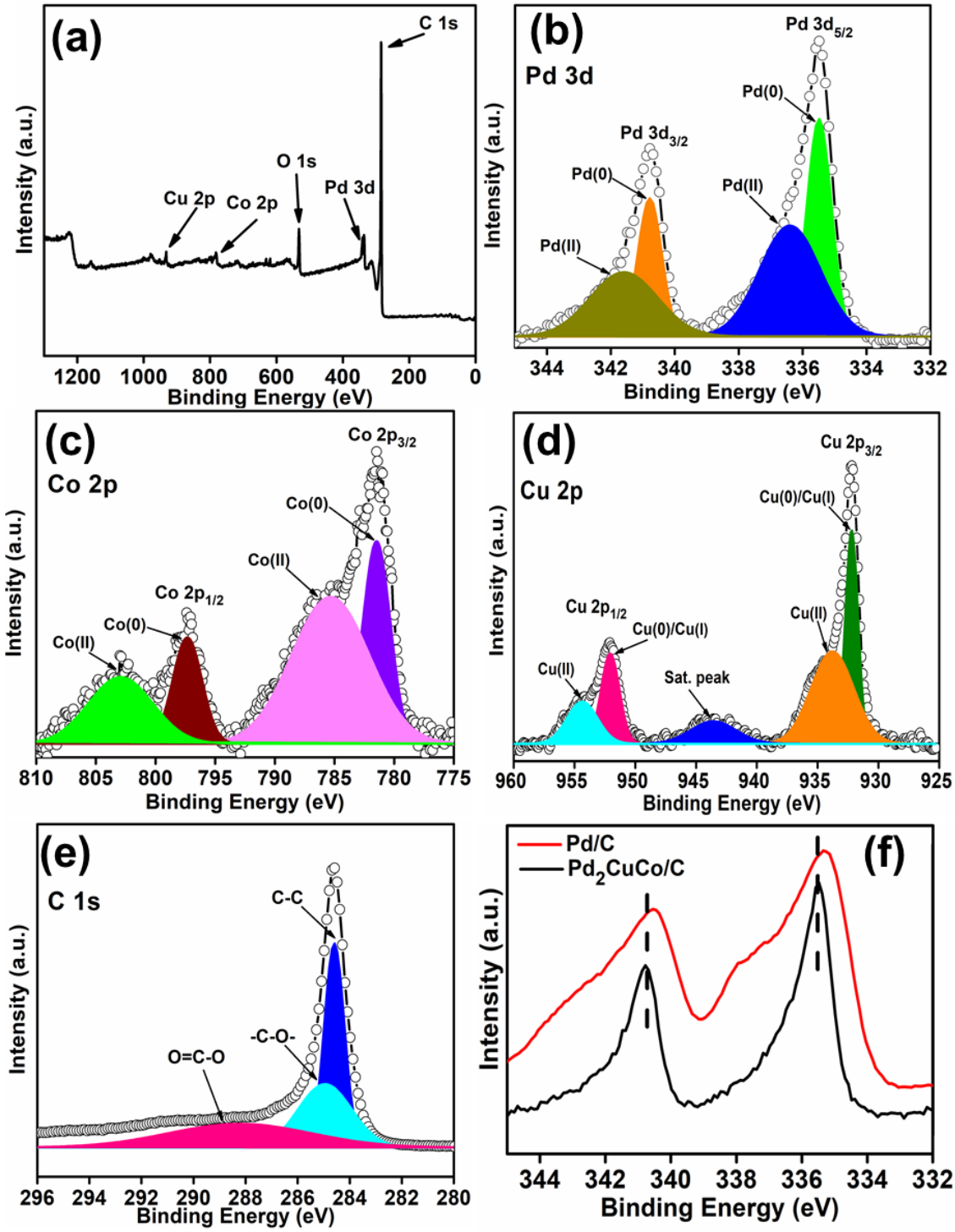

Figure 4.3: (a) XPS survey spectrum, high resolution XPS spectra of (b) Pd 3d, (c) Co 2p, (d) Cu 2p, and (e) C 1s of Pd_2CuCo/C, (f) correlation of binding energy change of Pd 3d of Pd_2CuCo/C and Pd/C.

The significant shift in BE in all the metals could be ascribed to strong electronic interactions between Pd, Co, and Cu during alloy formation [35]. The XP spectrum of C 1s of the Pd_2CuCo/C, owing to its asymmetry and presented in Figure 4.3e. The C 1s peak has three components (−C−C−, −C−O−, and O=C−O−) centered at 284.6, 286, and 289.9 eV, respectively. The strong intensity of the C-C bond indicates the presence of sp^3 carbon in the reported hybrid NPs [29, 38]. The Pd 3d spectrum of Pd/C and Pd_2CuCo/C when compared, a slight shift in Pd(0) $3d_{5/2}$ (335.3 eV) was noticed relative to pure Pd (BE=335.1 eV) (Figure 4.3f), which indicated the downshift of the Pd *d*-band center [32, 33]. The *d*-band center theory states that the charge transfer to Pd causes the Pd *d*-band center to shift downward, weakens the Pd-adsorbate interaction and thus enhances ORR electrocatalysis on the surface of Pd.

The TEM images of Pd_2CuCo/C at various resolutions are presented in Figures 4.4a and b. The spherical form of the metallic counterparts is uniformly distributed throughout the carbon matrix without aggregation, demonstrating the higher stability and less mass transfer resistance of the NPs. Homogeneous dispersion of metal NPs on carbon materials leads to higher catalytically exposed sites [28]. It is observed that a significant number of metal NPs homogeneously distributed over the carbon surface. More NPs dispersion leads to more active sites, thereby enhancing the electrocatalytic performance of the catalyst. Figure 4.4c shows that metal NPs are individually anchored on the carbon surface, forming strong metal-support interaction (SMSI). The HRTEM image revealed clear lattice fringes separated by 0.220 nm, 0.204 nm, and 0.208 nm, corresponding to the *fcc* plane of Pd (111), Cu (111), and Co (111), respectively (Figure 4.4d). These TEM results agree well with the XRD and XPS findings. The SAED pattern further indicates the sample's polycrystallinity that shows distinct concentric rings which matches well with the *fcc* structure of Pd (Figure 4.4e). Furthermore, the size and distribution of the NPs calculated using Image J software are shown in a histogram, as presented in Figure 4.4f. Most of the NPs were observed within the 5-8 nm range.

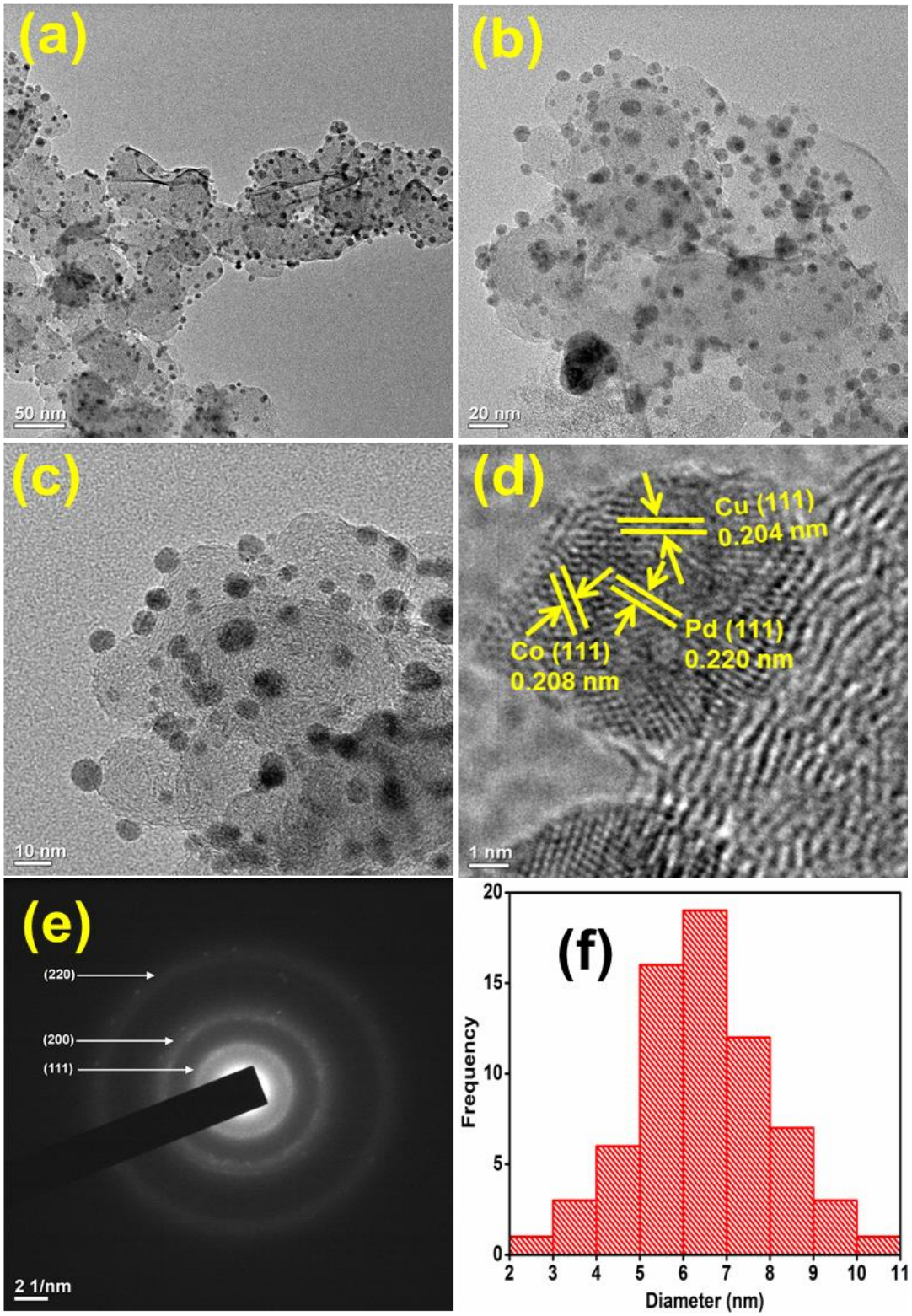

Figure 4.4: (a,b) low magnification transmission electron micrographs (TEM), (c,d) high resolution TEM (HRTEM) images, (e) the selected area of the electron diffraction (SAED) pattern, and (f) the corresponding particle size distribution of Pd_2CuCo/C (obtained from image (a)).

4.2.2. Electrocatalytic Activity towards ORR

CV and RDE measurements were used to evaluate the catalytic performance of the as-prepared Pd_2CuCo/C electrocatalyst. Figure 4.5a shows the CV plots of Pd_2CuCo/C in N_2- and O_2-saturated environments in KOH (0.1 M) solutions. Compared to the N_2-saturated peak, a significant and strong cathodic peak was observed in the CV graph in the O_2-saturated condition. This result indicates that the Pd_2CuCo/C electrocatalyst is active toward ORR. RDE measurements were done to evaluate the ORR kinetics in O_2-saturated KOH (0.1 M) electrolyte at varied rotation rates of 400-3600 rpm, as shown in Figure 4.5b. The polarization graph shows that when the rotation speed of the electrode rises, the current density also increases. The high oxygen diffusion rates are responsible for the increase in current density [39-41]. Figure 4.5c shows the Koutecky-Levich (K-L) plots obtained from the RDE graph in accordance with the equations denoted by equations (discussed in Chapter 2). The K-L plots are typically used to evaluate the kinetic current densities and the number (n) of electron transferred during the reduction reaction at different potentials. The K–L plots at different potentials display superb linearity and parallelism of Pd_2CuCo/C electrocatalysts, ensuring first-order ORR kinetics [42].

At different potentials ranging from 0.65 to 0.80V (*vs.* RHE), the average n values are calculated and found to be ~4 (inset in Figure 4.5c). So, the ORR on Pd_2CuCo/C electrocatalyst appears to follow a direct "$4e^-$" reduction pathway ($O_2 + 2H_2O + 4e^- = 4OH^-$) in alkaline electrolyte. The LSV curves at 1600 rpm were also recorded to compare the electrocatalytic performance of Pd_2CuCo/C with PdCu/C, PdCo/C, benchmark Pt/C and Pd/C (Figure 4.5d). Under identical conditions, the onset (E_{onset} = 0.91 V) and half-wave ($E_{1/2}$ = 0.806 V) potentials of Pd_2CuCo/C are highly positive than the other counterparts, implying that Pd_2CuCo/C has greater ORR activity. Additionally, the Pd_2CuCo/C electrocatalyst shows a higher limiting current density (j_m) value of -5.65 $mAcm^{-2}$ than the PdCu/C (-4.5 $mAcm^{-2}$), PdCo/C (-4.9 $mAcm^{-2}$), Pd/C (-2.47 $mAcm^{-2}$) and Pt/C (-5.5 $mAcm^{-2}$).

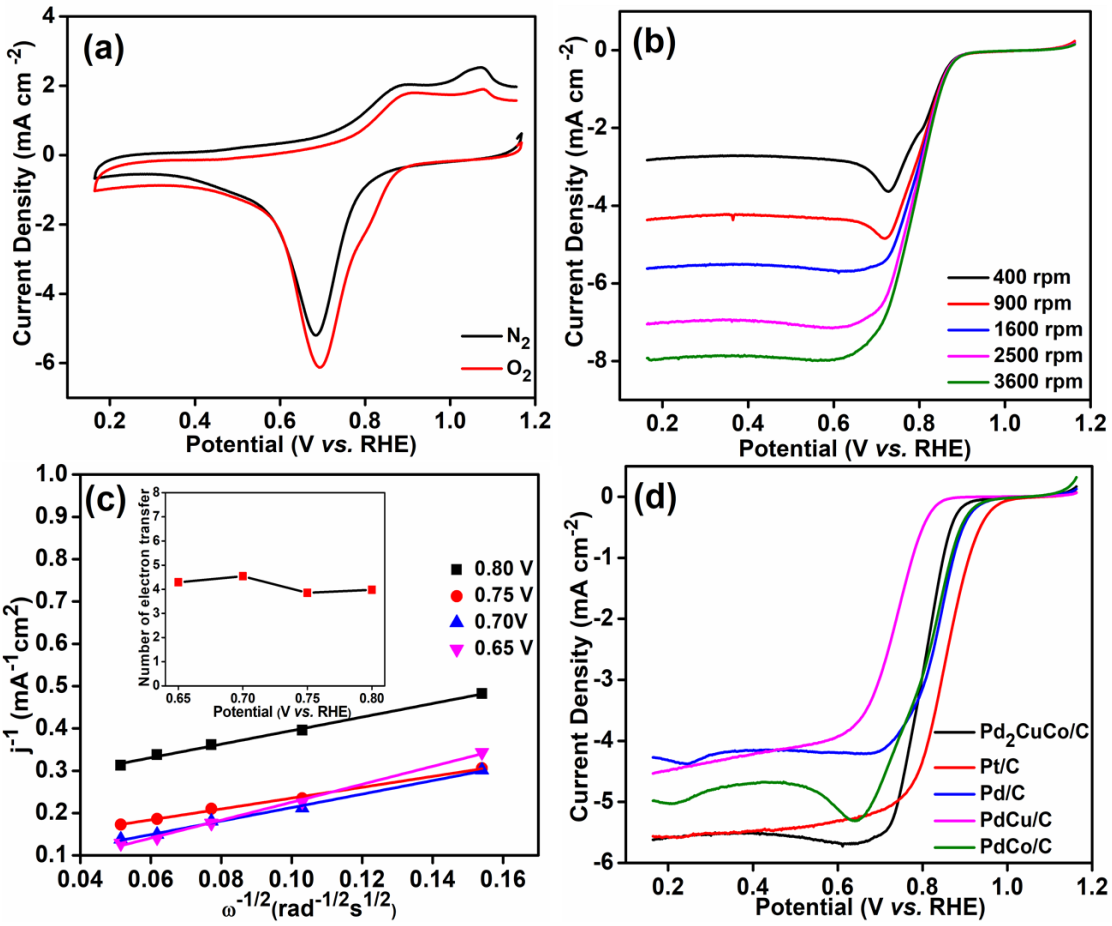

Figure 4.5: (a) CV recorded in N_2- and O_2-saturated 0.1 M KOH solution with a scan rate at 50 mVs^{-1}, (b) ORR polarization LSV recorded in O_2-saturated 0.1 M KOH with scan rate 10 mVs^{-1}, (c) corresponding Koutecky-Levich plot at different potentials, (inset: electron transfer number (n) *vs.* potential for Pd_2CuCo/C), (d) comparison of ORR polarization LSV plots of Pd_2CuCo/C, Pt/C, Pd/C, PdCu/C and PdCo/C in O_2-saturated 0.1 M KOH solution, rotational speed: 1600 rpm.

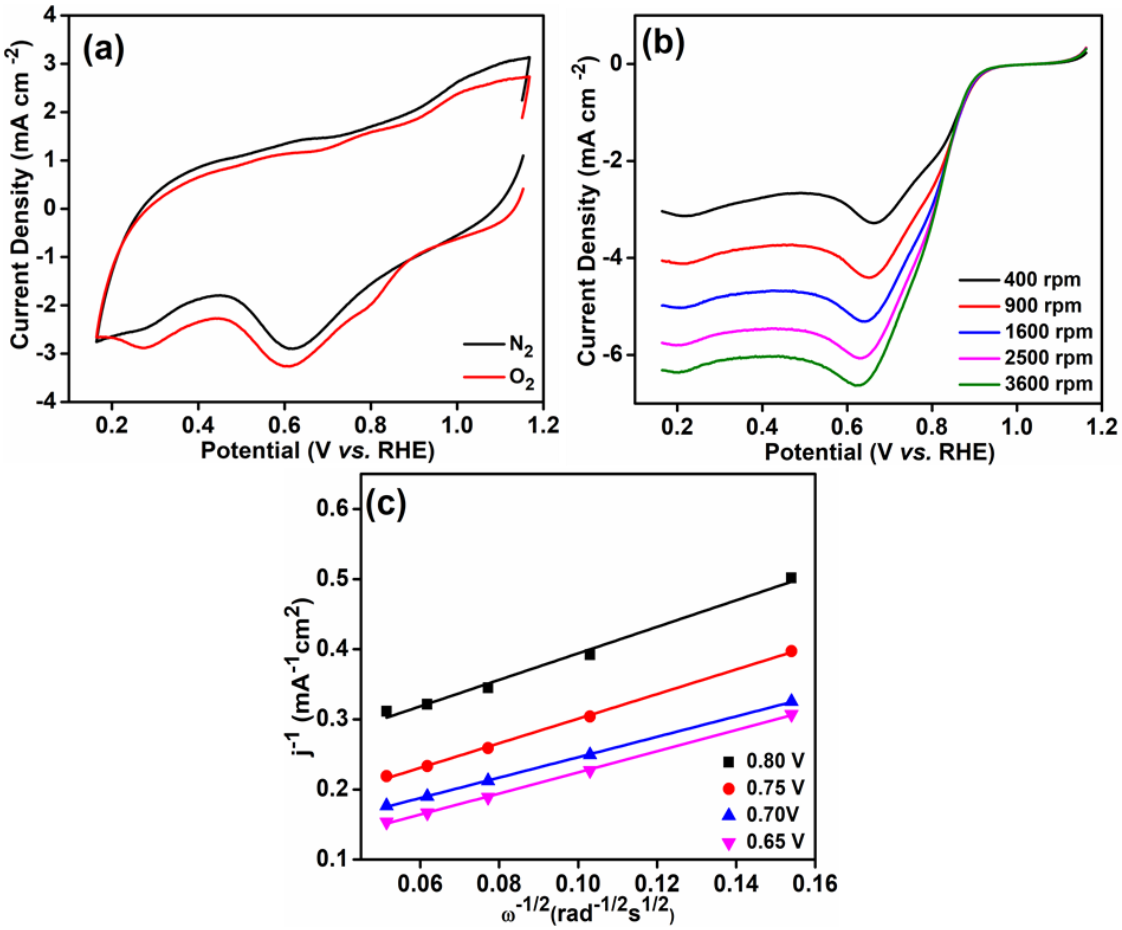

Figure 4.6: (a) CV plots of PdCo/C, N_2- and O_2-saturated 0.1 M KOH solution with a scan rate of 50mVs^{-1}, (b) rotating rate-dependent ORR polarization curves for respective electrocatalyst with the scan rate of 10 mVs^{-1}, (c) corresponding Koutecky-Levich plot at different potentials.

To compare the electrocatalytic performance of catalysts, CV and LSV analyses of PdCo/C and PdCu/C were also carried out in N_2 and O_2-saturated 0.1 M KOH solution and presented in Figure 4.6 and 4.7. The LSV curves at different rotation increases with increase in the rotating speed presented in Figure 4.6b and 4.7b, similar behaviors were observed for Pd_2CuCo/C. The corresponding KL plot at various potentials in the mixed controlled regions for PdCo/C and PdCu/C are also plotted and presented in Figures 4.6c and 4.7c, respectively. A series of linear and parallel lines were observed for both PdCo/C and PdCu/C.

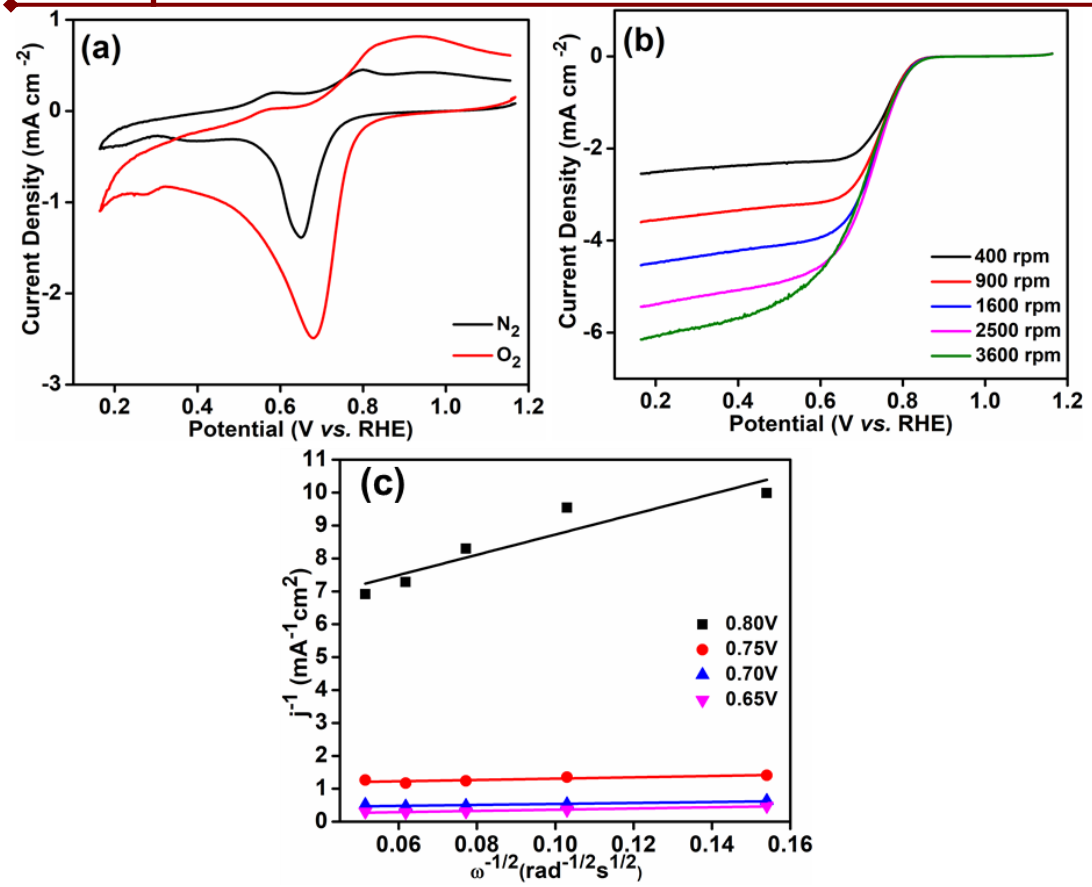

Figure 4.7: (a) CV plots of PdCu/C, N_2- and O_2-saturated 0.1 M KOH solution with a scan rate of 50 mVs^{-1}, (b) rotating rate-dependent ORR polarization curves for respective electrocatalyst with the scan rate of 10 mVs^{-1}, (c) corresponding Koutecky-Levich plot at different potentials.

A comparison of E_{onset}, $E_{1/2,}$ and j_m values of all the electrocatalysts is presented in Table 4.1. From the table, it is pertinent although the kinetics of Pd_2CuCo/C might not be the earliest, once it gets started; it generates higher currents than the other electrocatalysts. The $E_{1/2}$ values of Pd_2CuCo/C, PdCu/C, PdCo/C, Pt/C and Pd/C are 0.806V, 0.74V, 0.805V, 0.858 and 0.81V *vs.* RHE, respectively. The j_m of Pd_2CuCo/C (-5.65 $mAcm^{-2}$) is 1.25 and 1.15 times higher than the PdCu/C (-4.5 $mAcm^{-2}$) and PdCo/C (-4.9 $mAcm^{-2}$), respectively. The commendable performance of Pd_2CuCo/C may be attributed to more active sites present on the surface of the electrocatalyst, indicates better dispersion of the NPs over the carbon matrix and stronger synergistic effect between Pd, Cu and Co.

Table 4.1: Summary of, $E_{1/2}$, j_m and ECSA of Pd_2CuCo/C, Pt/C, Pd/C, PdCu/C and PdCo/C for ORR

Sl No.	**Electrocatalysts**	**$E_{1/2}$ (V *vs.* RHE)**	**J_m (mA cm^{-2})**	**ECSA (m^2g^{-1})**
1	Pd_2CuCo/C	0.806	-5.65	132.9
2	Pt/C	0.858	-5.5	29.5
3	Pd/C	0.81	-2.47	21.7
4	PdCu/C	0.74	-4.5	72.8
5	PdCo/C	0.805	-4.9	83.9

The CV plots of the synthesized electrocatalysts, including PdCu/C, PdCo/C, Pt/C, and Pd/C in N_2-saturated 0.1M KOH electrolyte recorded at a scan rate of 50 mVs^{-1} (Figure 4.8a). This CV curve represents that Pd_2CuCo/C has a higher positive reduction potential than PdCu/C and PdCo/C. The increments of reduction potential are due to the incorporation of both Cu and Co in the Pd lattice, which lowers the lattice distance and increases ORR activity by decreasing the adsorption energy of intermediates. From this CV plot, the electrochemically active surface area (ECSA) of all the reported catalysts was calculated, and it is an essential factor for determining the actual active sites present in the catalysts. ECSA is different from the BET surface area, which provides an entire surface area of the catalyst even though not all accessible surfaces may be electrochemically active. The procedure for calculation of ECSA is described in Chapter 2. The ECSA values follows the order Pd_2CuCo/C (132.9 m^2g^{-1}) > PdCo/C (83.9 m^2g^{-1}) > PdCu/C (72.8 m^2g^{-1}) > Pt/C (29.5 m^2g^{-1}) > Pd/C (21.7 m^2g^{-1}). The ECSA value of Pd_2CuCo/C is 1.58, 1.82, 4.5 and 6.1 times larger than the PdCo/C, PdCu/C, Pt/C and Pd/C, respectively. An increased ECSA means more electrochemically active sites are on the catalyst surface, and this is attributed to the SMSI caused by the uniform dispersion of metallic particles on the carbon support, as inferred from the TEM image.

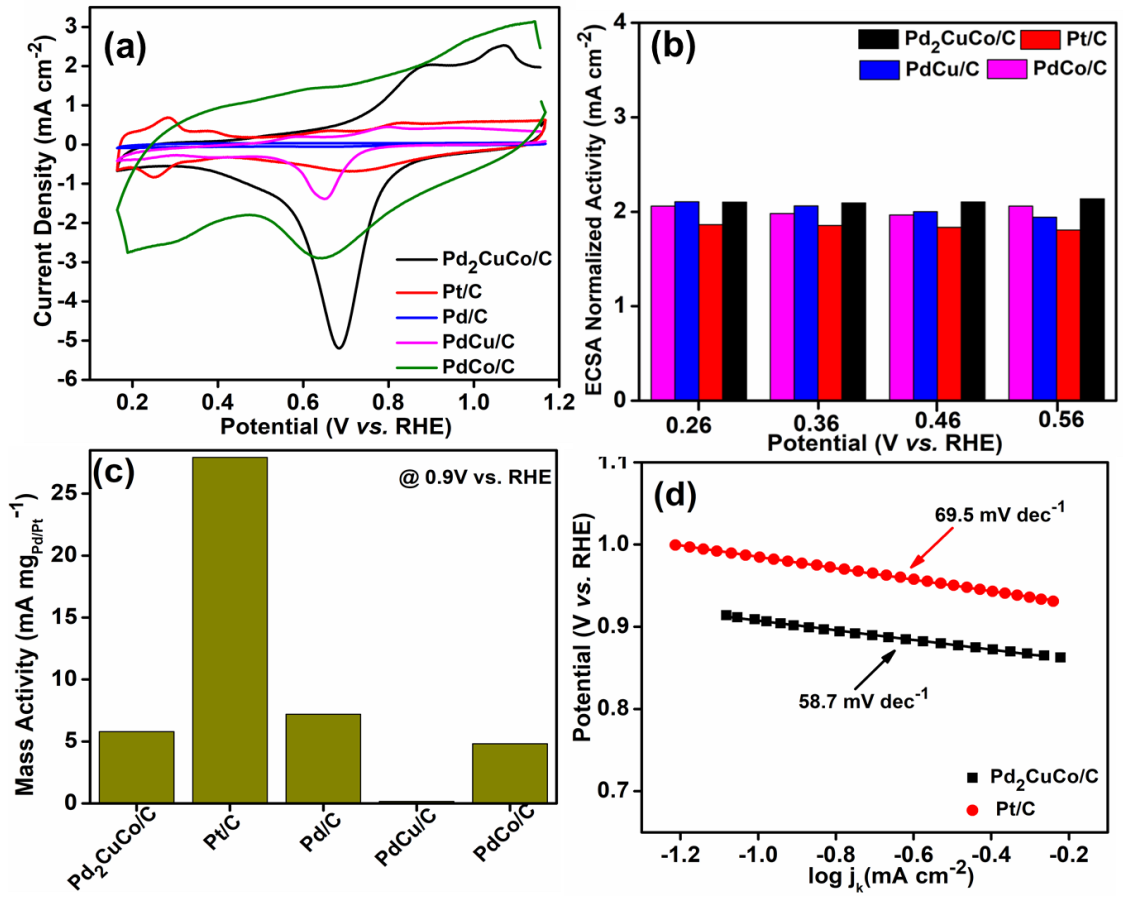

Figure 4.8: (a) CV of Pd_2CuCo/C, Pt/C, Pd/C, PdCu/C and PdCo/C electrocatalyst recorded in N_2-saturated 0.1 M KOH with a sweep rate of 50 mVs^{-1}, (b) ECSA normalized activity under varied potentials for Pt/C, PdCu/C, PdCo/C, and Pd_2CuCo/C electrocatalysts, (c) mass activities (MA) for Pd/C, Pt/C, PdCu/C and PdCo/C and Pd_2CuCo/C electrocatalysts at 0.9V *vs*. RHE and (d) corresponding Tafel plots obtained from LSV curves of Pt/C and Pd_2CuCo/C electrocatalysts.

The ECSA normalized activity and mass activity (MA) of all the reported electrocatalysts were determined and presented in Figure 4.8b and c. The mass MA and ECSA normalized activity were measured by normalizing the kinetic current to the active mass of Pt or Pd loading and to the ECSA of the catalysts. As shown in Figure 4.8c, MA at 0.90 V *vs.* RHE for Pd_2CuCo/C was found to be ~1.4 and 34.3 times higher than PdCo/C and PdCu/C, respectively. The superior MA and ECSA normalized activity of Pd_2CuCo/C ascribed to more dispersion of metal NPs on the carbon surface and more active sites, as reflected from the ECSA. To further understand the kinetics of the catalysts, the Tafel slope value was determined by linearly fitting the polarization curve,

shown in Figure 4.8d. Notably, a low value of the Tafel slope is associated with a slight increase in potential, a higher electrocatalytic current density, and a higher catalytic efficiency. The Pd_2CuCo/C has a lower Tafel slope (58.7 mV dec^{-1}) relative to commercial Pt/C (69.5 mV dec^{-1}) suggesting a higher catalytic efficiency with a faster electron transfer rate of Pd_2CuCo/C toward ORR.

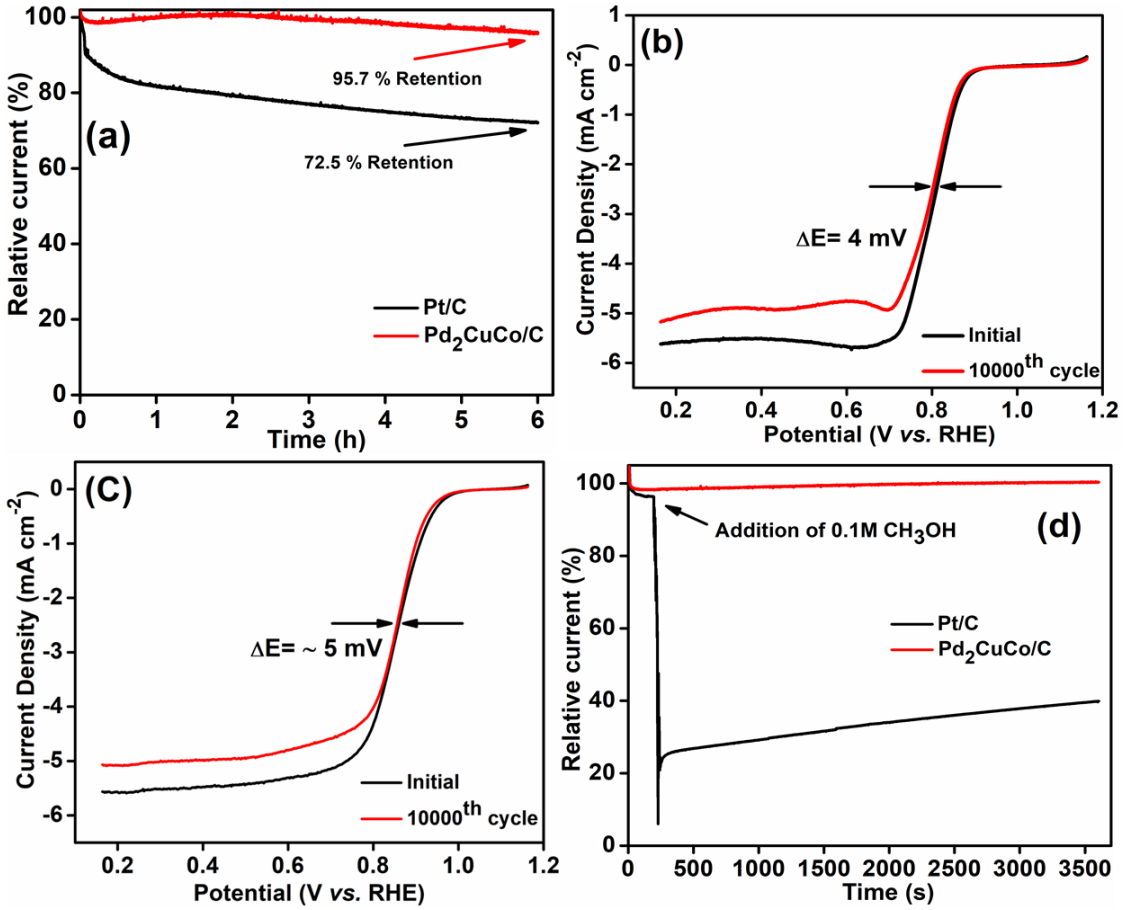

Figure 4.9: (a) Chronoamperometry (CA) plots of stability test of Pd_2CuCo/C and Pt/C measured at 0.66 V (*vs.* RHE) in O_2-saturated 0.1 M KOH solution, rotational speed: 1600 rpm, ORR polarization LSV plots of (b) Pd_2CuCo/C, and (c) Pt/C at 1600 rpm before and after 10000 cycles, (d) CA curves of a methanol tolerance test of Pd_2CuCo/C and Pt/C for 3600 s.

Long-term stability and durability are essential criteria for the practical application of electrocatalysts. A chronoamperometry (CA) test was done to assess the electrochemical stability of the Pd_2CuCo/C, as illustrated in Figure 4.9a. The initial

current decay for Pt/C is 27.5% after 6 h, whereas the current decay for Pd_2CuCo/C is just 4.3%, indicating the Pd_2CuCo/C's exceptional stability. To further verify the durability of the reported electrocatalysts, accelerated durability test (ADT) was performed for 10000 cycles in O_2-saturated 0.1 M KOH electrolyte in the potential ranging from 0.2, and 1.20 V (*vs.* RHE) at 500 mVs^{-1} and compared with Pt/C and the data was presented in Figure 4.9b and c, respectively. The E_{onset} for both Pd_2CuCo/C and Pt/C are nearly unchanged after 10000 cycles, and only 4 mv of a negative shift in $E_{1/2}$ for Pd_2CuCo/C is observed which is lower than the Pt/C. We conclude from these comparative investigations that the reported Pd_2CuCo/C catalyst has better ORR catalytic activity than the commercial Pt/C. The remarkable ORR performance of Pd_2CuCo/C may be due to the electronic effects of including Cu and Cu metal in the Pd lattice. The Pd_2CuCo/C and benchmark Pt/C catalyst's tolerance to methanol were also studied. As demonstrated in Figure 4.9d, the ORR current of the Pd_2CuCo/C electrode did not significantly change after the addition of methanol at 200s. Contrarily, the Pt/C electrocatalyst's ORR current drops dramatically, indicating that Pd_2CuCo/C has a remarkable ORR selectivity and a good capacity for avoiding the crossover effect. These outcomes further support the Pd_2CuCo/C electrocatalyst’s potential for direct methanol and alkaline FC applications.

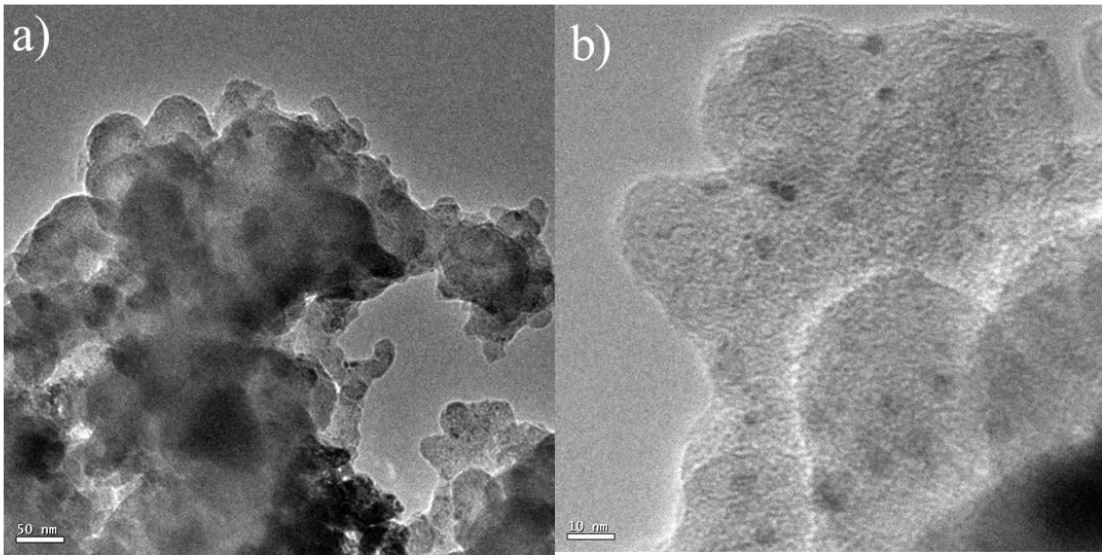

Figure 4.10: (a) Low-resolution and (b) high-resolution TEM images of Pd_2CuCo/C post-catalytic samples, respectively.

To ascertain the morphology and structure of the catalyst, TEM analysis was done after this long-term stability test. Figure 4.10 represents the low-resolution and high-resolution TEM images of Pd_2CuCo/C. The robustness of investigated catalysts is evident from the TEM images that show no significant morphological and structural changes which demonstrate the excellent structural integrity of Pd_2CuCo/C. The Pd_2CuCo NPs are homogeneously distributed over carbon support after this long hour of electrostability test.

Table 4.2 displayed the electrocatalytic performance comparison with some Pd-based catalysts that had been previously published. The ORR performance demonstrated by the Pd_2CuCo/C NPs was found to be superior to those of a few recently reported catalysts. The ORR onset potential of Pd_2CuCo/C is excellent compared to that of Pd-g-C_3N_4 [44] and PtPd alloy networks [45]. Similarly, the Pd_2CuCo/C exhibits superior half-wave potential than most of the reported electrocatalysts such as $Pd_1Ni_1Cu_{0.8}/C$ [46], Au@Pd/rGO [47], G−Cu_3Pd [49] and GN@Pd-GA [54]. Moreover, the as-synthesized electrocatalysts displayed much lower Tafel slope (58.7 mV dec^{-1}) than the other enlisted electrocatalysts and very close to $Co_{0.2}Sn_{0.2}Pd_{0.2}/rGO$ [48]. These results show that Pd_2CuCo/C has the best intrinsic activity among these reported catalysts. Furthermore, we have compared the ECSA value, which would be responsible for a notable improvement in the electrocatalyst's catalytic performance, for a better understanding of the factors underlying the catalyst's high ORR performance. Pd_2CuCo/C exhibits a higher ECSA value than several electrocatalysts [25, 28, 29, 44-55], indicating the presence of more catalytic active sites on the surface of Pd_2CuCo/C. These superior catalytic performances make the Pd_2CuCo/C nanostructure a potential electrocatalyst toward ORR.

Furthermore, in accordance with Chapter 3, it was observed that the stability and durability are superior or comparable with low Pd content. In this chapter, we have a 50% of Pd loading in a total 20% metallic part, whereas in the previous chapter, it was a 75% of Pd loading in a total 20% metallic part. With a 25% lower Pd content than in Chapter 3 ($Pd_3Ag_{0.5}Cu_{0.5}/C$), the present catalyst displays commendable performance for ORR. Therefore, it can be concluded that introducing Cu and Co in the Pd lattice effectively disperses the metallic counterparts over the entire support, leading to superior performance.

Table 4.2: Comparison of the ORR parameters of Pd-based electrocatalysts in 0.1 M KOH

Electrocatalysts	**E_{onset} V (*vs.* RHE)**	**$E_{1/2}$ V (*vs.* RHE)**	**Tafel slope (mV dec^{-1})**	**ECSA (m^2g^{-1})**	**References**
Pd_2CuCo/C	0.91	0.806	58.7	132.9	This work
PtPdCu tripods	1.00	0.94	60	39.2	25
Pd_2CuCo/C NF	0.94	0.82	67.83	100.9	28
Pd_3Ni	0.96	0.84	71.4	120.7	29
Pd-g-C_3N_4	0.90	0.70		67.6	44
PtPd alloy networks	0.89			38.6	45
$Pd_1Ni_1Cu_{0.8}/C$		0.757			46
Au@Pd/rGO	0.961	0.761			47
$Co_{0.2}Sn_{0.2}$ $Pd_{0.2}$ /rGO		0.91	57		48
G–Cu_3Pd		0.785	68.9		49
G-AuPd@Pd	0.95	0.87		93.5	50
Pd_4Au HCs/C	1.00	0.87	65	5.9	51
v-Pd_2CoAg	0.95		66		52
$Co_5Fe_2Pd_1$	0.97	0.87	74		53
GN@Pd-GA	0.92	0.76			54
PdCuCo-AS		0.901		70.4	55

4.3. Conclusions

In summary, we have successfully synthesized a Pd_2CuCo alloy uniformly anchored on Vulcan carbon through a modified solvothermal process. The evaluation of the electrocatalytic activity of Pd_2CuCo alloy toward ORR indicated a positive E_{onset} and $E_{1/2}$, along with excellent redox durability and long-term stability. Additionally, the electrocatalyst displayed superior MeOH tolerance than the benchmark Pt/C. The excellent electrocatalytic performances of the Pd_2CuCo alloy were assumed due to the uniform dispersion over the carbon matrix that provided a large surface area and improved active sites. The results indicate that these electrocatalysts may be applied as a novel candidate with lower Pd content than the commercial Pd/C, which is cost-effective and highly efficient for ORR applications in energy conversion devices.

References

[1] Pan, M., Pan, C., Li, C., Zhao, J. A review of membranes in proton exchange membrane fuel cells: transport phenomena, performance and durability. *Renewable Sustainable Energy Review*, 141:110771, 2021.

[2] Xiao, F., Wang, Y.C., Wu, Z.P., Chen, G., Yang, F., Zhu, S., Siddharth, K., Kong, Z., Lu, A., Li, J.C., Zhong, C.J. Recent advances in electrocatalysts for proton exchange membrane fuel cells and alkaline membrane fuel cells. *Advanced Materials*, 33(50):2006292, 2021.

[3] Shao, M., Chang, Q., Dodelet, J.P., Chenitz, R. Recent advances in electrocatalysts for oxygen reduction reaction. *Chemical Reviews*, 116(6):3594-3657, 2016.

[4] Patowary, S., Chetry, R., Goswami, C., Chutia, B., Bharali, P. Oxygen reduction reaction catalysed by supported nanoparticles: Advancements and challenges. *ChemCatChem*, 14(7):e202101472, 2022.

[5] Kim, J.W., Lim, B., Jang, H.S., Hwang, S.J., Yoo, S.J., Ha, J.S., Cho, E.A., Lim, T.H., Nam, S.W., Kim, S.K. Size-controlled synthesis of Pt nanoparticles and their electrochemical activities toward oxygen reduction. *International Journal of Hydrogen Energy*, 36(1):706-712, 2011.

[6] Esmaeilifar, A., Rowshanzamir, S., Eikani, M.H., Ghazanfari, E. Synthesis methods of low-Pt-loading electrocatalysts for proton exchange membrane fuel cell systems. *Energy*, 35(9):3941-3957, 2010.

[7] Stamenkovic, V.R., Mun, B.S., Arenz, M., Mayrhofer, K.J., Lucas, C.A., Wang,

G., Ross, P.N., Markovic, N.M. Trends in electrocatalysis on extended and nanoscale pt-bimetallic alloy surfaces. *Nature Materials*, 6(3):241-247, 2007.

[8] Lin, J.Y., Xi, C., Li, Z., Feng, Y., Wu, D.Y., Dong, C.K., Yao, P., Liu, H., Du, X.W. Lattice-strained palladium nanoparticles as active catalysts for the oxygen reduction reaction. *Chemical Communications*, 55(21):3121-3123, 2019.

[9] Xu, H., Shang, H., Wang, C., Du, Y. Recent progress of ultrathin 2D Pd-based nanomaterials for fuel cell electrocatalysis. *Small*, *17*(5):2005092, 2021.

[10] Roy, N., Yasmin, S., Ejaz, A., Han, H.S., Jeon, S. Influence of pyrrolic and pyridinic-n in the size and distribution behaviour of Pd nanoparticles and orr mechanism. *Applied Surface Science*, 533:147500, 2020.

[11] Ju, W., Favaro, M., Durante, C., Perini, L., Agnoli, S., Schneider, O., Stimming, U., Granozzi, G. Pd nanoparticles deposited on nitrogen-doped HOPG: New insights into the Pd-catalyzed oxygen reduction reaction. *Electrochimica Acta*, 141:89-101, 2014.

[12] Chen, A., Ostrom, C. Palladium-based nanomaterials: Synthesis and electrochemical applications. *Chemical Reviews*, 115:11999−12044, 2015.

[13] Lu, Y., Jiang, Y., Gao, X., Wang, X., Chen, W. Strongly coupled Pd nanotetrahedron/tungsten oxide nanosheet hybrids with enhanced catalytic activity and stability as oxygen reduction electrocatalysts. *Journal of the American Chemical Society*, 136:11687−11697, 2014.

[14] Luo, Y., Yang, Q., Nie, W., Yao, Q., Zhang, Z., Lu, Z. H. Anchoring IrPdAu nanoparticles on NH_2-SBA-15 for fast hydrogen production from formic acid at room temperature. *ACS Applied Materials & Interfaces*, 12:8082−8090, 2020.

[15] Wang, W., Zhao, Y., Ding, Y. 2D ultrathin core–shell $Pd@Pt_{monolayer}$ nanosheets: Defect-mediated thin film growth and enhanced oxygen reduction performance. *Nanoscale*, 7:11934-11939, 2015.

[16] Xue, Q., Xu, G., Mao, R., Liu, H., Zeng, J., Jiang, J., Chen, Y. Polyethyleneimine modified AuPd@PdAu alloy nanocrystals as advanced electrocatalysts towards the oxygen reduction reaction. *Journal of Energy Chemistry*, 2017, *26*, 1153-1159.

[17] Wang, C., Chen, D.P., Sang, X., Unocic, R.R., Skrabalak, S.E., Size-dependent disorder–order transformation in the synthesis of monodisperse intermetallic PdCu nanocatalysts. *ACS Nano*, 10(6):6345-6353, 2016.

[18] Huang, K., Hui, Y., Yang, Z., Waqas, M., Fan, F., Wang, L., Liu, X., Huang, Q., Huang, D., Chen, D.H., Fan, Y. N, S co-doped carbon film wrapped Co nanoparticles for boosting oxygen reduction reaction. *Molecular Catalysis*, 541:113102, 2023.

[19] Zhong, J. P., Hou, C., Sun, M.L., Yang, Z.Y., Chen, D.H., Fan, Y.J., Chen, W., Liao, H.G., Sun, S.G. A superior electrocatalyst toward the oxygen reduction reaction obtained by atomically dispersing copper on N, F co-doped graphene through atomic interface engineering. *Journal of Materials Chemistry A*, 10:13876-13883, 2022.

[20] Peng, C., Hu, Y., Liu, M., Zheng, Y. Hollow Raspberry-like PdAg alloy nanospheres: High electrocatalytic activity for ethanol oxidation in alkaline media. *Journal of Power Sources*, 278:69-75, 2015.

[21] Li, X., Huang, Q., Zou, Z., Xia, B., Yang, H. Low temperature preparation of carbon-supported PdCo alloy electrocatalysts for methanol-tolerant oxygen reduction reaction. *Electrochimica Acta*, 53:6662−6667, 2008.

[22] Shi, J., Qiu, F., Yuan, W., Guo, M., Lu, Z. H. Nitrogen-doped carbon-decorated yolk-shell CoP@FeCoP micro-polyhedra derived from MOF for efficient overall water splitting. *Chemical Engineering Journal*, 403:126312, 2021.

[23] Wang, H., Yin, S., Li, Y., Yu, H., Li, C., Deng, K., Xu, Y., Li, X., Xue, H., Wang, L. One-step fabrication of tri-metallic PdCuAu nanothorn assemblies as an efficient catalyst for oxygen reduction reaction. *Journal of Materials Chemistry A*, 6(8):3642-3648, 2018.

[24] Zhen, C., Lyu, Z., Liu, K., Chen, X., Sun, Y., Liao, X., Xie, S. Ultrasmall PdPtCo trimetallic nanorings with enriched low-coordinated edge sites and optimized compositions for effective oxygen reduction electrocatalysis. *CrystEngComm*, 23(29):5033-5038, 2021.

[25] Wang, H., Yin, S., Xu, Y., Li, X., Alshehri, A.A., Yamauchi, Y., Xue, H., Kaneti, Y.V. Wang, L. Direct fabrication of tri-metallic PtPdCu tripods with branched exteriors for the oxygen reduction reaction. *Journal of Materials Chemistry A*, *6*(18):8662-8668, 2018.

[26] Zhu, Y., Wang, S., Luo, Q., Huang, H., Tang, S., Du, Y. Facile synthesis of structurally ordered low-Pt-loading Pd–Pt–Fe nanoalloys with enhanced electrocatalytic performance for oxygen reduction reaction. *Journal of Alloys and*

Compounds, 855:157322, 2021.

[27] Kong, F., Liu, S., Li, J., Du, L., Banis, M.N., Zhang, L., Chen, G., Doyle-Davis, K., Liang, J., Wang, S., Zhao, F. Trimetallic Pt–Pd–Ni octahedral nanocages with subnanometer thick-wall towards high oxygen reduction reaction. *Nano Energy*, 64:103890, 2019.

[28] Borah, B.J., Goswami, C., Yamada, Y., Tada, K., Tanaka, S., Bharali, P. Pd_2CuCo/C hybrid with nanoflower morphology toward oxygen reduction and formic acid oxidation reactions: experimental and computational studies. *Energy & Fuels*, 35(14):11515-11524, 2021.

[29] Goswami, C., Saikia, H., Tada, K., Tanaka, S., Sudarsanam, P., Bhargava, S. K., Bharali, P. Bimetallic palladium–nickel nanoparticles anchored on carbon as high-performance electrocatalysts for oxygen reduction and formic acid oxidation reactions. *ACS Applied Energy Materials*, 3(9):9285-9295, 2020.

[30] Wang, Y., Gan, R., Ai, Z., Liu, H., Wei, C., Song, Y., Dirican, M., Zhang, X., Ma, C., Shi, J. Hollow Co_3O_{4-x} nanoparticles decorated n-doped porous carbon prepared by one-step pyrolysis as an efficient orr electrocatalyst for rechargeable zn-air batteries. *Carbon*, 181:87-98, 2021.

[31] Lv, H., Guo, X., Sun, L., Xu, D., Liu, B. A universal strategy for fast, scalable, and aqueous synthesis of multicomponent Palladium alloy ultrathin nanowires. *Science China Chemistry*, 64(2):245-252, 2021.

[32] Li, Z., Li, J., Jiang, K., Yuan, S., Yu, D., Wei, H., Shi, Z., Li, X., Chu, H. PdCoNi alloy nanoparticles decorated, nitrogen-doped carbon nanotubes for highly active and durable oxygen reduction electrocatalysis. *Chemical Engineering Journal*, 411:128527, 2021.

[33] Liu, X., Fu, G., Chen, Y., Tang, Y., She, P., Lu, T. Pt-Pd-Co trimetallic alloy network nanostructures with superior electrocatalytic activity towards the oxygen reduction reaction. *Chemistry: A European Journal*, 20(2):585-590, 2014.

[34] Bin, D., Yang, B., Ren, F., Zhang, K., Yang, P., Du, Y. Facile synthesis of pdni nanowire networks supported on reduced graphene oxide with enhanced catalytic performance for formic acid oxidation. *Journal of Materials Chemistry A*, *3*(26):14001-14006, 2015.

[35] Li, C., Yuan, Q., Ni, B., He, T., Zhang, S., Long, Y., Gu, L., Wang, X. Dendritic Defect-rich palladium–copper–cobalt nanoalloys as robust multifunctional non-

platinum electrocatalysts for fuel cells. *Nature Communications*, 9(1):3702, 2018.

[36] Li, X.C., She, F.S., Shen, D., Liu, C.P., Chen, L.H., Li, Y., Deng, Z., Chen, Z.H., Wang, H.E. Coherent nanoscale cobalt/cobalt oxide heterostructures embedded in porous carbon for the oxygen reduction reaction. *RSC Advances*, 8(50):28625-28631, 2018.

[37] Xu, L., Li, J., Sun; H., Guo, X., Xu, J., Zhang; H., Zhang, X. In situ growth of Cu_2O/CuO nanosheets on Cu coating carbon cloths as a binder-free electrode for asymmetric supercapacitors. *Frontiers in Chemistry*, 7:420, 2019.

[38] Chen, X., Wang, X., Fang, D. A Review on C 1s XPS-spectra for some kinds of carbon materials. *Fuller. Nanotub. Carbon Nanostructures*, 28(12):1048-1058, 2020.

[39] Singh, H., Marley-Hines, M., Chakravarty, S., Nath, M. Multi-walled carbon nanotube supported manganese selenide as a highly active bifunctional OER and ORR electrocatalyst. *Journal of Materials Chemistry A*, 10(12):6772-6784, 2022.

[40] Zhou, M., Wang, H.L., Guo, S. Towards high-efficiency nanoelectrocatalysts for oxygen reduction through engineering advanced carbon nanomaterials. *Chemical Society Reviews*, 45(5):1273-1307, 2016.

[41] Li, Q., Xu, P., Zhang, B., Tsai, H., Zheng, S., Wu, G., Wang, H.L. Structure-dependent electrocatalytic properties of Cu_2O nanocrystals for oxygen reduction reaction. *The Journal of Physical Chemistry C*, 117(27):13872-13878, 2013.

[42] Liu, R., Wu, D., Feng, X., Müllen, K. Nitrogen-doped ordered mesoporous graphitic arrays with high electrocatalytic activity for oxygen reduction. *Angewandte Chemie International Edition*, 49(14):2565-2569, 2010.

[43] Borah, B. J., Saikia, H., Goswami, C., Hazarika, K. K., Yamada, Y., Bharali, P. Unique half embedded/exposed PdFeCu/C interfacial nanoalloy as high-performance electrocatalyst for oxygen reduction reaction. *ChemCatChem*, 11:3522−3529, 2019.

[44] Konda, S.K., Amiri, M., Chen, A. Photoassisted deposition of palladium nanoparticles on carbon nitride for efficient oxygen reduction. *The Journal of Physical Chemistry C*, 120(27):14467-14473, 2016.

[45] Shi, Y.C., Mei, L.P., Wang, A.J., Yuan, T., Chen, S.S., Feng, J.J. L-Glutamic acid assisted eco-friendly one-pot synthesis of sheet-assembled platinum-palladium alloy networks for methanol oxidation and oxygen reduction reactions. *Journal of*

Colloid and Interface Science, 504:363-370, 2017.

[46] Sun, L., Liao, B., Ren, X., Li, Y., Zhang, P., Deng, L., Gao, Y. Ternary PdNi-based nanocrystals supported on nitrogen-doped reduced graphene oxide as highly active electrocatalysts for the oxygen reduction reaction. *Electrochimica Acta*, 235:543-552, 2017.

[47] Li, S.S., Wang, A.J., Hu, Y.Y., Fang, K.M., Chen, J.R., Feng, J.J. One-Step, seedless wet-chemical synthesis of gold@palladium nanoflowers supported on reduced graphene oxide with enhanced electrocatalytic properties. *Journal of Materials Chemistry A*, 2(43):18177-18183, 2014.

[48] Wang, H., Li, L., Sheng, S., Wang, C., Qu, T., Hou, D., Wang, D., Sheng, M. Synthesis of low-cost Co-Sn-Pd/rGO catalysts via ultrasonic irradiation and their electrocatalytic activities toward oxygen reduction reaction. *The Canadian Journal of Chemical Engineering*, 100:S160-S171, 2022.

[49] Zheng, Y., Zhao, S., Liu, S., Yin, H., Chen, Y.Y., Bao, J., Han, M., Dai, Z. Component-controlled synthesis and assembly of Cu–Pd nanocrystals on graphene for oxygen reduction reaction. *ACS Applied Materials & Interfaces*, 7(9):5347-5357, 2015.

[50] Zheng, J.N., Li, S.S., Ma, X., Chen, F.Y., Wang, A.J., Chen, J.R., Feng, J.J. Green synthesis of core–shell gold–palladium@palladium nanocrystals dispersed on graphene with enhanced catalytic activity toward oxygen reduction and methanol oxidation in alkaline media. *Journal of Power Sources*, 262:270-278, 2014.

[51] Jiao, W., Chen, C., You, W., Zhao, X., Zhang, J., Feng, Y., Wang, P., Che, R. Hollow palladium-gold nanochains with periodic concave structures as superior orr electrocatalysts and highly efficient SERS substrates. *Advanced Energy Materials*, 10(18):1904072, 2020.

[52] Liu, S., Zhang, H., Mu, X., Chen, C. Surface reconstruction engineering of twinned Pd_2CoAg nanocrystals by atomic vacancy inducement for hydrogen evolution and oxygen reduction reactions. *Applied Catalysis B: Environmental*, 241:424-429, 2019.

[53] Wang, C., Qu, T., Wang, D., Kang, Z. Synthesis of Co-Fe-Pd nanoparticles via ultrasonic irradiation and their electro-catalytic activity for oxygen reduction reaction. *Applied Catalysis A: General*, 560:103-110, 2018.

[54] Zuo, Y., Rao, D., Li, S., Li, T., Zhu, G., Chen, S., Song, L., Chai, Y., Han, H.

atomic vacancies control of Pd-based catalysts for enhanced electrochemical performance. *Advanced Materials*, 30(1):1704171, 2018.

[55] Wu, X.T., Li, J.C., Pan, Q.R., Li, N., Liu, Z.Q. Gallic acid-assisted synthesis of Pd uniformly anchored on porous N-rGO as efficient electrocatalyst for microbial fuel cells. *Dalton Transaction*, 47(5):1442-1450, 2018.